The International Journal of **Medical Robotics** and **Computer Assisted Surgery**

THE INTERNATIONAL JOURNAL OF MEDICAL ROBOTICS AND COMPUTER ASSISTED SURGERY
Int J Med Robotics Comput Assist Surg 2013; **9**: 230–239.
Published online 21 March 2013 in Wiley Online Library (wileyonlinelibrary.com) **DOI:** 10.1002/rcs.1494

ORIGINAL ARTICLE

A remote-controlled vascular interventional robot: system structure and image guidance

Cai Meng[1]*
Jun Zhang[1]
Da Liu[2]
Bo Liu[1]
Fugen Zhou[1]

[1]*Image Processing Centre, Beihang University, Beijing, People's Republic of China*

[2]*Robotics Institute, Beihang University, Beijing, People's Republic of China*

*Correspondence to: Cai Meng, Image Processing Centre, Beihang University, 37 Xueyuan Road, Beijing 100191, People's Republic of China.
E-mail: Tsai@buaa.edu.cn

Accepted: 28 January 2013

Abstract

Background Robot-assisted vascular interventional surgery (VIS) enables the surgeon to teleoperate a catheter in a safe cabinet, such that exposure to X-ray radiation is reduced. For safe and accurate teleoperation, system structure and image guidance is important.

Methods The system structure of the developed remote-controlled vascular interventional robot (RVIR) and its image guidance system (IGS) are introduced. RVIR is based on a master–slave structure. Key technologies of IGS are addressed, including C-arm calibration, distortion correction, catheter localization and 3D vasculature reconstruction.

Results Experiments show that the RMS error of distortion correction is 0.35 pixels, and 0.53 mm for distance reconstruction. The error in catheter localization between the IGS and the encoders is small. *In vitro* and *in vivo* tests verified the feasibility of RVIR.

Conclusions Experiments indicate that the RVIR is feasible and valid to help the surgeon perform VIS remotely; the function and reconstruction accuracy of IGS can satisfy the surgeon's requirement to guide the RVIR. Copyright © 2013 John Wiley & Sons, Ltd.

Keywords vascular interventional robot; image guidance; C-arm calibration; 3D reconstruction

Introduction

In traditional vascular interventional surgery (VIS), an experienced surgeon inserts the catheter into the patient's artery and propels it to the target vascular branch under the image guidance of a digital subtraction angiography (DSA) machine. However, neither X-ray nor DSA images provide three-dimensional (3D) information. When the catheter arrives at a complex vascular structure, e.g. a vascular bifurcation, the surgeon often needs to repeat the insertion attempts to let the catheter enter into the right branch. This may tear the blood vessel at the junction and result in bleeding (1). It also results in a longer X-ray exposure time, which is harmful to both the patient and the surgeon.

Medical robots have played an important role in helping the doctor perform minimal invasive surgery because of their stability and high accuracy (2–6). The vascular interventional robot enables the surgeon to teleoperate the catheter in a safe place, and therefore protects the surgeon from exposure to X-ray irradiation (3,4). Furthermore, under the help of 3D reconstruction and visualization technologies, the surgeon can perform the VIS more

effectively and reduce the X-ray exposure time to the patient. Remote operated robot-assisted vascular intervention surgery has a broad application prospect (7).

Several robotic systems for interventional therapy have been developed in recent years. Guo *et al*. (4)designed a master–slave catheter operating system for medical applications. A simple micro force sensor was used to ensure the safety of the whole system. Their experimental results indicated that it could effectively improve the operability into aneurysm with force feedback for intravascular neurosurgery. Saliba *et al*. (8)introduced a robotic catheter remote control system to facilitate control and precise positioning of the catheters within the cardiovascular system; the catheter was controlled via a master–slave electromechanical system. Jayender *et al*. (9)studied the image guidance for robot-assisted catheter insertion; they showed that active catheter insertion could be autonomously guided without any doctor's assistance. In the above system, the surgeon manipulated the catheter under the guidance of two-dimensional (2D) DSA images. Compared with 2D images, a 3D vasculature model can provide spatial information, especially at the vascular bifurcation, and overlap in the DSA image. Tercero *et al*. (10) proposed a system for tracking the position and speed of a catheter, using a magnetic motion capture sensor to provide feedback to a catheter-driving mechanism, to perform autonomous catheter insertion in major vasculature. They also presented epoxy-resin as a material for vasculature modelling and developed quantitative evaluation methods for the catheter trajectory inside vasculature phantoms. Meanwhile, a catheter trajectory reconstruction method that used a biplanar optical vision system was introduced. They also provided 3D visualization of the stress within the blood vessel and of the guide wire, 3D approximation of catheter shape and vasculature model morphology (11–13). Liu *et al*. (14) integrated a bidirectional steerable catheter with two magnetic position-tracking sensors and developed a visualization interface to provide catheterization with a 3D guiding image; their system is able to provide 3D guidance but is time-consuming, since a series of isolated guiding circular planes were set along the navigation path.

We also developed a remote-controlled vascular interventional robot (RVIR), based on a C-arm DSA machine, and conducted several *in vitro* and *in vivo* tests. RVIR has the following characteristics:

1. The robot consists of a supporting manipulator and a catheter navigator. The supporting manipulator holds the catheter navigator to adjust its position.
2. IGS can reconstruct the 3D vasculature model from the 2D DSA images, thus providing 3D visualization of the vasculature model for the surgeon.
3. IGS can locate the catheter tip and show its displacement to the surgeon.
4. The surgeon can teleoperate the catheter with a force-feedback control device via the catheter navigator.
5. A micro force sensor is mounted on the catheter tip and the haptic force can be fed back to the surgeon to prevent piercing the blood vessel wall.

In this paper, the system structure of the RVIR and the key technologies of IGS are addressed. The paper is arranged as follows: At first, the system structure of RVIR and IGS are introduced; secondly, the methods of C-arm calibration and DSA image distortion correction are described; thirdly, we introduce the procedures of catheter localization and 3D vascular model reconstruction; fourthly, several experiments are conducted to test the efficacy and accuracy of the IGS and RVIR; and finally, we discuss and briefly summarize our work.

Materials and methods

System structure

The designed system structure of the RVIR is shown in Figure 1, which is a master–slave structure. The master site lies in an isolated cabinet with a protective lead glass window. At the master site, there is a remote control device and a graphic workstation with two LCDs. The remote control device is a three- degree of freedom (DOF) Falcon haptic device from Novint Technologies, which provides the surgeon with a direct human computer interface (HCI) to control the catheter and feel the haptic force feedback between the catheter tip and the blood vessel wall. IGS runs in the graphic workstation and provides a 3D vasculature model, X-ray images and catheter tip location information for the surgeon to guide the procedure.

The slave site lies in the operating room. There are a rotational C-arm-based DSA machine, a binocular optical tracker, the medical robot and an operating bed. The binocular optical tracker provides a world reference frame and is used to trace and locate the position and orientation of the C-arm and the robot. The medical robot consists of two parts, a supporting manipulator and a catheter navigator. The supporting manipulator can be locked to an arbitrary posture, which makes up a passive hydraulic mechanism. The catheter navigator is fixed at the end of the supporting manipulator. It consists of many gears and a drum and can drive different kinds of catheter for axial and rotational movements. The catheter is designed in a special way and its tail is equipped with a micro force sensor that can sense the touch force. The feedback force provides real resistance for the surgeon to prevent injuring the blood vessels effectively (15).

Image guidance system

IGS plays an important role in assisting the surgeon to perform VIS. It supplies 2D fluoroscopic images, 3D visualization

DOI: 10.1002/rcs

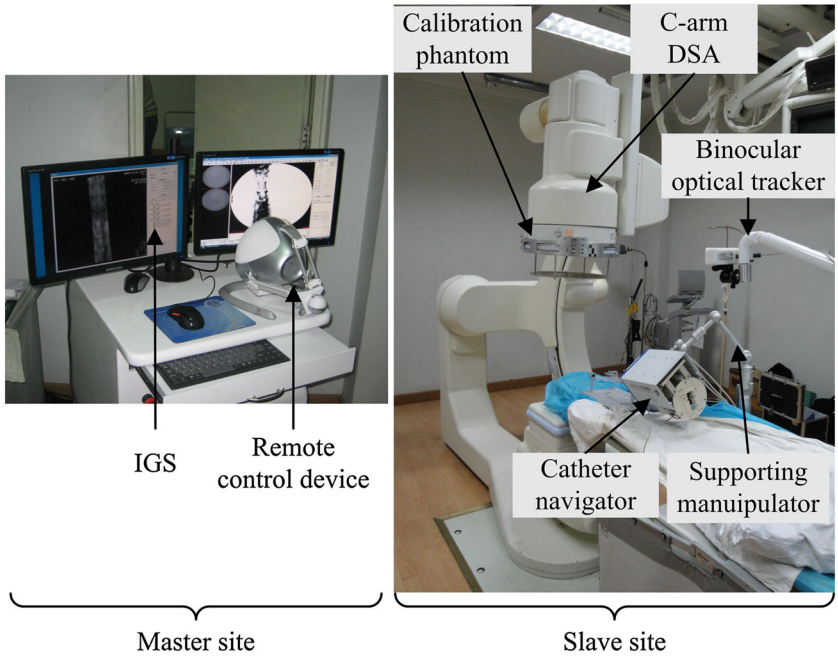

Figure 1. Structure of RVIR.

of the vasculature model and quantitative information about the catheter tip to the surgeon. The workflow of the RVIR is shown in Figure 2 and the function of the IGS is marked out by dotted rectangle frame.

The procedure can be divided into pre- and intra-operation stages. In the pre-operation stage, the C-arm imaging system is calibrated with a calibration phantom at not less than two predefined view positions. In the intra-operation stage, the procedure is carried out by the following steps:

1. Acquisition and correction of the DSA images of the patient at the predefined view positions.
2. Extraction of blood vessel from the corrected DSA images and reconstruction of its 3D model.
3. Insertion of a catheter into the artery from the entry point chosen by the surgeon and correction of the catheter's X-ray images for localization.
4. Teleoperation of the catheter via RVIR by the surgeon to perform the procedure, based on the 3D vasculature model and the catheter's spatial position information.

During the interventional procedure, the surgeon can adjust catheter movements according to the haptic force between the catheter and the blood vessels, which is measured by the micro force sensor. This helps the surgeon avoid piercing the blood vessel wall.

To provide catheter localization and 3D vasculature model for the surgeon, the imaging parameters of the C-arm should be calibrated in IGS and the DSA images should be corrected.

Automatic match of marker images with their space positions

C-arm calibration builds the relationship between the images and their coordinates in the world frame and determines the distortion parameters. To calibrate the C-arm, markers should be used whose coordinates in world frame and in image are known or worked out and which should also correspond. In order to acquire these correspondences, a calibration phantom is designed.

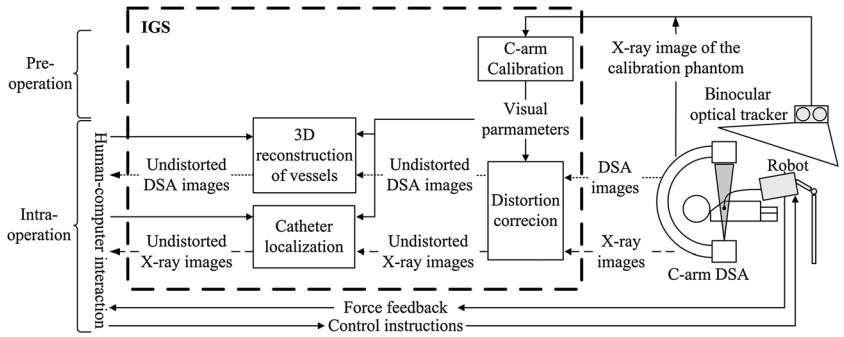

Figure 2. The workflow of RVIR.

A double-layered aluminium calibration phantom is designed as illustrated in Figure 3. It consists of two parallel thin plates. In the lower layer, arrays of holes are spaced with the same interval. In the upper layer, there are nine holes which correspond vertically to the nine holes on the lower layer. These holes work as markers and they are all small, except for three large holes *A*, *B* and *C* in the lower. Since the phantom should be removed after calibration and the number of visible markers varies in every mount, an automatic method should be developed to extract the marker images and match them with their coordinates in the world frame.

In the phantom, we can build a local right-hand reference frame by the markers *A*, *B* and *C*, i.e. taking *A* as the origin, *AB* as the *x* axis and *AC* as the *y* axis (Figure 4). Since these three holes are bigger than other holes and distances between them differ obviously, they can be distinguished in the X-ray image. Let *a*, *b* and *c* be their image points. With *a*, *b* and *c*, we can build an affine coordinate frame on the distorted C-arm image. Then the corresponding spatial positions of these image markers can be automatically configured using the following steps:

1. Extracting the marker images and calculating their subpixel positions. This can be realized by using the morphological image processing technique and centroid calculation. Based on their subpixel positions, they are rounded to the nearest integer to get their affine coordinates in the above-mentioned affine coordinate frame.
2. Building the homography between the image affine plane and the plane of the lower layer of the phantom. The homography can be determined by the correspondence of markers *A*, *B*, *C* and *M* and their images *a*, *b*, *c*, and *m*.
3. Calculating the image markers' corresponding spatial positions in the local frame, based on the above homography. The image of upper layer markers can be distinguished by applying adjacent neighbour and sequence constraints.
4. Transforming the spatial positions from local frame to world frame. On the phantom there is a known optical marker with three *X* corners, *E*, *F* and *G*, pasted at predefined position on the phantom. It can also be localized by the binocular optical tracker system, which works as the world frame. Therefore, the transformation between local frame and world frame can be determined.

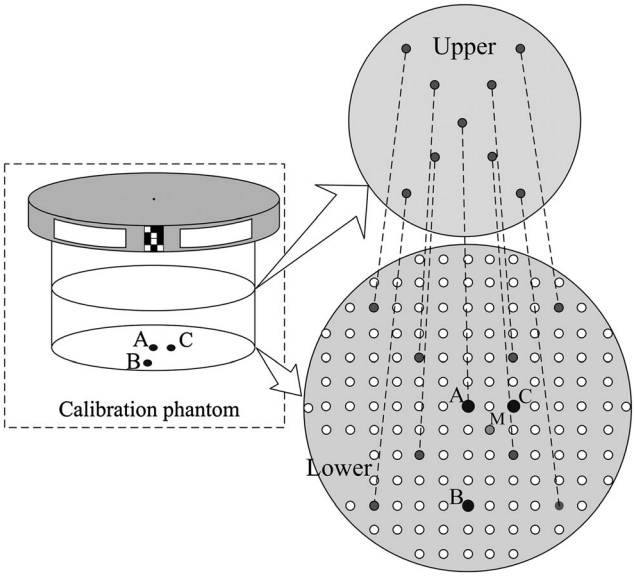

Figure 3. Double-layered aluminum calibration phantom.

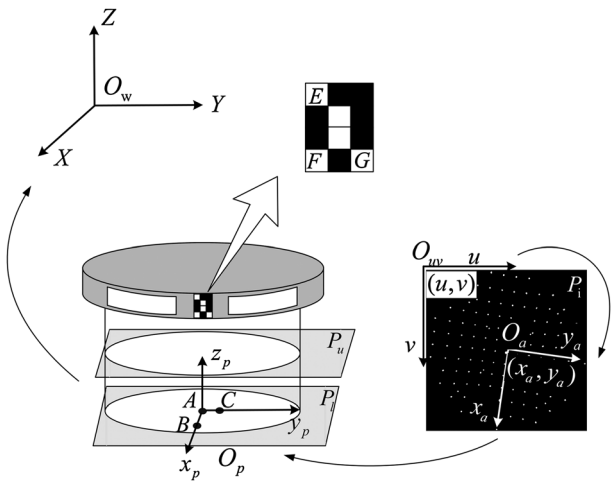

Figure 4. Transformations between different coordinate systems.

C-arm calibration

The ideal model of the C-arm imaging system is a pinhole camera model (16). However, the real C-arm image includes three main geometrical distortions: pincushion distortion, sigmoidal distortion and local distortion (17). The local distortion model is rather complex (18). Generally it is very small and is negligible in most research (19). Therefore we neglect it too. Let $\mathbf{p}$ be the ideal image point of spatial point *P*, and $\mathbf{p}_d$ the actual distorted image point. $\mathbf{p}_d$ is dependent on the C-arm image distortion and can be described as:

$$\mathbf{p}_d = \mathbf{p} + \boldsymbol{\delta}\ \boldsymbol{\delta} = \boldsymbol{\delta}_p + \boldsymbol{\delta}_s \tag{1}$$

where $\boldsymbol{\delta}$ is the sum of geometrical distortions, including the pincushion distortion $\boldsymbol{\delta}_p$ and the sigmoidal distortion $\boldsymbol{\delta}_s$.

The pincushion distortion is modelled as radial distortion as in Tsai's method (20)

$$\begin{cases} \delta_{px} = x_i\left(k_1 r^2 + k_3 r^4 + k_5 r^6 + \ldots\right) \\ \delta_{py} = y_i\left(k_2 r^2 + k_4 r^4 + k_6 r^6 + \ldots\right) \end{cases}, r = \sqrt{x_i^2 + y_i^2} \tag{2}$$

where (x_i, y_i) is the ideal position and $k_1, k_2, k_3, \ldots$ are the coefficients of pincushion distortion. In the IGS, the 2nd polynomial is considered, therefore k_1 and k_2 are kept.

DOI: 10.1002/rcs

The sigmoidal distortion is dependent on the orientation of the C-arm in magnetic fields. It changes considerably when the C-arm is rotated to different positions. We model the sigmoidal by considering the translation and displacement effect:

$$\begin{cases} \delta_{sx} = (x_i \cos\theta - y_i \sin\theta)(1 + t/r) - x_i \\ \delta_{sy} = (x_i \sin\theta + y_i \cos\theta)(1 + t/r) - y_i \end{cases} \quad (3)$$

where θ and t are the magnitude of rotational and translational effect.

As sigmoidal distortion is localized, the rotational and translational distortions vary at different positions. A polynomial is used to describe this characteristic. θ, t, k_1 and k_2 are computed by the following equation separately:

$$\sum_{p=0}^{n} \sum_{q=0}^{n-p} a_{pq} x_i^p y_i^q \quad (4)$$

where n is the polynomial degree and a_{pq} is the polynomial coefficient.

Based on the distortion model and the correspondence between image points and their spatial positions, the C-arm imaging system can be calibrated using a non-linear optimization method. For non-linear optimization, a proper initial value should be provided for fast and stable convergence. In C-arm images, sigmoidal distortions are much smaller compared with pincushion distortion at the central regions. Therefore the method of Tsai (20) is used to estimate the initial parameters of the C-arm with correspondences within the central region. In our method, the central region is defined as the central part of the image with radius of one-quarter of the image side length.

Note that these parameters are applied to the central region of the image instead of the whole image. Let the initial value of the sigmoidal distortion parameters be **0**. The parameters can be propagated to the whole image by non-linear optimization with correspondence data in the whole image. The Levenberg–Marquadt algorithm is chosen here to minimize the physical distance between the actual distorted positions and their calculated distorted positions.

Distortion correction

After calibration, the distorted image can be corrected by using back-projection, based on the distortion model. C-arm image correction involves three main steps:

1. Generating a blank image with the same size of distorted C-arm image, which works as ideal image.
2. Calculating the mapping between the ideal image and the distorted C-arm image for every pixel, based on the distortion model and the calibrated distortion parameters.
3. For any pixel in the ideal image, if its corresponding distorted position exceeds the original real C-arm image, then its grey value is set at 0, else its pixel value is interpolated with neighbouring pixels around its corresponding distorted position in the real C-arm image. In the IGS, a bilinear interpolation algorithm is utilized.

Catheter localization and 3D vascular reconstruction

After C-arm calibration and image correction, any spatial location of point P can be recovered by its image points, like traditional stereovision, as shown in Figure 5. Based on point reconstruction, the catheter localization and 3D vasculature model can be reconstructed.

Epipolar geometric constraints

Epipolar geometry provides effective constraints in searching for image correspondence in reconstruction. In Figure 5, $\mathbf{p}_1$ and $\mathbf{p}_2$ are image points of spatial point P in C-arm images at two predefined views. Epipolar constraint indicates that $\mathbf{p}_2$ must lie on its epipolar line, l, which is determined by $\mathbf{p}_1$, and a fundamental matrix **F**. **F** is a matrix that can be determined by eight image point correspondences (21).

To automatically calibrate **F**, a small phantom (Figure 6) was designed, which is made up of synthetic glass plate and has 20 steel balls of different diameters. These steel

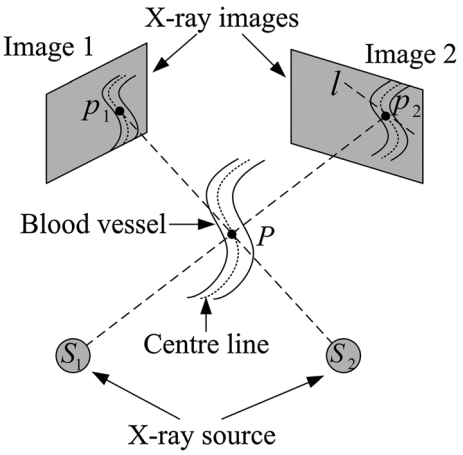

Figure 5. Epipolar geometry.

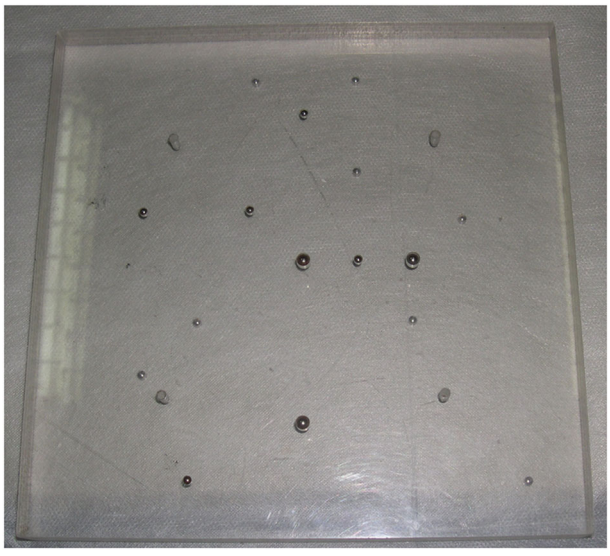

Figure 6. Small phantom for calibrating the fundamental matrix.

DOI: 10.1002/rcs

balls are placed on three planes, where three large ones are on the same plane and the other small ones are distributed on other planes. Assuming I_1 and I_2 to be the small phantom's images viewed from two positions, **F** can be calibrated by the correspondence of the ball image in I_1 and I_2. Viewed from the central polar coordinate system, the relative size of angular coordinates of these balls keeps the same sequence. This characteristic is used to match the balls' images in I_1 and I_2 automatically. The matched result is shown in Figure 7, where matched points have the same serial number.

Catheter localization and 3D vascular reconstruction

A 3D view of the vasculature model and the catheter is useful for the surgeon when the catheter meets the bifurcation of a blood vessel. Reconstruction of a blood vessel (or catheter) comprises five major steps:

1. Acquiring DSA images I_1 and I_2 at the two predefined view positions.
2. Correcting I_1 and I_2, based on the C-arm calibration to eliminate the distortion.

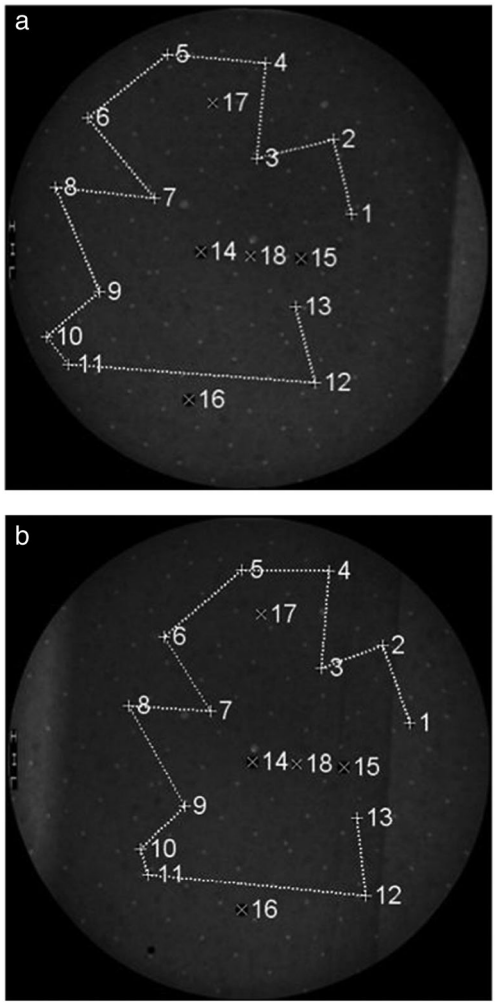

Figure 7. Points automatic matching.

3. Constructing the blood vessel structure. Because of the low image quality of DSA images, it is hard to reconstruct the blood vessel structure automatically. Therefore, an interactive segmentation method, 'live-vessel', is adopted (22). The surgeon determines a source point as the start of a vascular branch. Then, the optimal path between the source point and the current position is calculated and displayed when the surgeon moves the cursor. If the path is suitable, it will be fixed and the control point will become a new source point. This step continues until the surgeon picks an ending point. The interactive segmentation is repeated branch by branch. Finally, the blood vessel structure is constructed (Figure 8).
4. Matching the vascular centre line. The extracted blood vessels trend nearly along the vertical direction in DSA images, while the tendencies of epipolar lines are almost along the horizontal direction. Hence, a 'horizontal' epipolar line and the 'vertical' vascular intersect at one point. If a point p_1 on the vascular centre line in image I_1 is selected, its epipolar line $\boldsymbol{l}$ in image I_2 can be calculated. The intersection of $\boldsymbol{l}$ and the vascular centre line in image $\boldsymbol{I}_2$ is the corresponding point of $\boldsymbol{p}_1$. If there is more than one intersection, then other constraints should be considered to eliminate mismatches.
5. 3D vasculature model reconstruction. Based on the vascular centre line point correspondences and the C-arm calibrated projection matrixes, a 3D vasculature skeleton tree can be constructed. Suppose the cross-section of a blood vessel is round, then its diameter can be figured out according to its vasculature width in the image by reversing the geometric magnification.

The 3D catheter can be reconstructed in a similar way, except that X-ray images are used instead of DSA images. At the catheter tip there is a small metal ring, therefore it can be visualized in X-ray images.

Intervention navigation

The IGS in RVIR enables 3D roadmap view by overlapping the vasculature model on real-time fluoroscopic images (as in Figure 9). This helps the surgeon to choose the best view from precalibrated projection views to acquire X-ray images with minimal foreshortening and overlapping. Moreover, a 3D model of the catheter can be displayed,

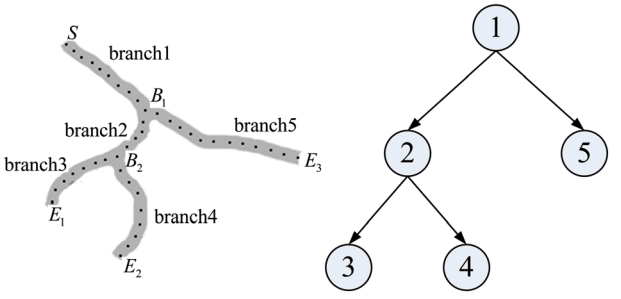

Figure 8. Vessel tree construction. The blood vessel has five branches. Point *S* is the start point; 1 *B* and 2 *B* are bifurcation points; 1 *E* , 2 *E* and 3 *E* are ending points.

DOI: 10.1002/rcs

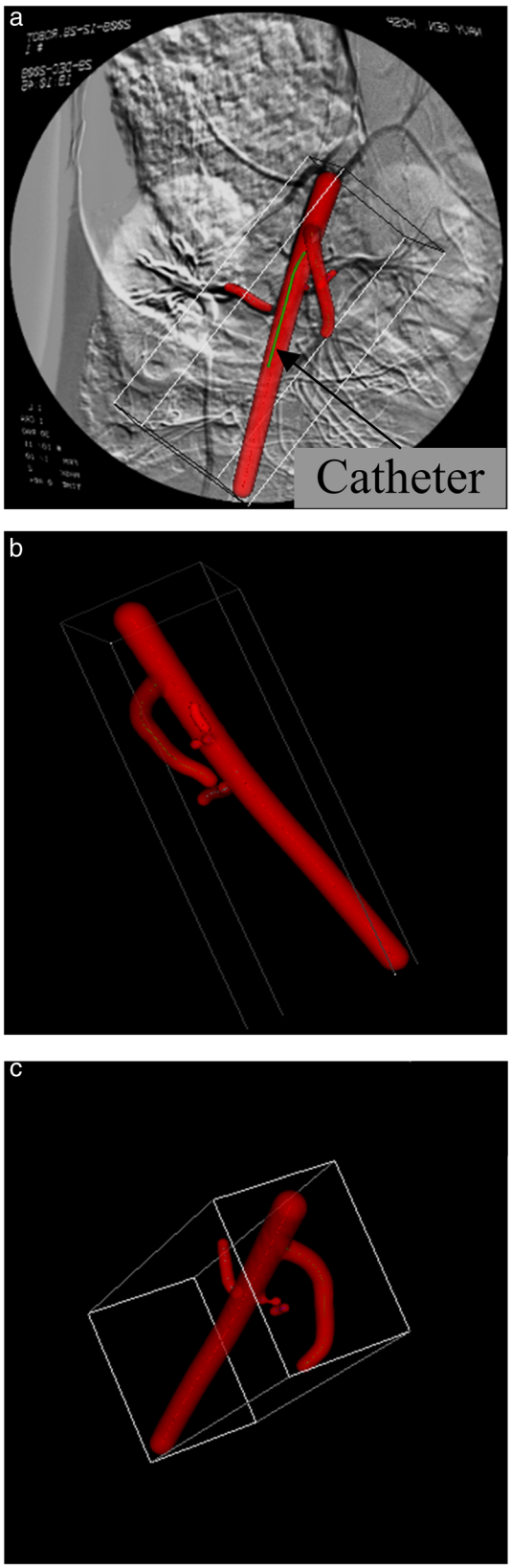

Figure 9. Different IGS views. (a)Overlap of the 3D vasculature model and catheter on 2D monitoring image; (b)(c) Different views of 3D vasculature model.

together with the 2D blood vessel image. In this way, the information would give the surgeon a better understanding of the vascular structure and its geometric relationship with the catheter.

Several views of IGS are depicted in Figure 9 (the renal artery of a canine). In order to show the quality of the reconstructed model, Figure 9 shows the reconstructed vascular model observed from three different views. From the 3D roadmap view, the 3D vascular model matches the projection perfectly according to the accurate C-arm calibration beforehand.

Experiments and results

In order to verify the validity of the RVIR and IGS, different tests have been conducted, including distortion correction, spatial distance reconstruction, catheter localization and clinical simulation. These experiments were conducted at the Chinese Navy General Hospital, where a GE LCV C-arm with a 12' fluorescent screen is employed and a H40 Microntracker is used as the binocular optical tracker. The experimental platform is shown in Figure 1. To recover 3D information, two C-arm views at $\alpha = 0^\circ$, $\beta = 0^\circ$ (α is the primary angle of the C-arm and β is the secondary angle) and $\alpha = 30^\circ$, $\beta = 0^\circ$ were chosen, and the images captured at the two views were noted as I_0 and I_{30}.

Distortion correction error

In this experiment, we tested the error of the proposed distortion correction method. At first, the calibration phantom was attached on the C-arm. Then X-ray images were captured at predefined views, respectively. After automatic markers image extraction and automatic matching with their space positions, the C-arm imaging system was calibrated at these two views. Based on the calibrated parameters, the images could be corrected. However, in the test we reprojected the spatial markers to the image to figure out their theoretical distorted positions based on the proposed distortion model. The error of distortion correction was indicated by the differences between these markers' real positions in the distorted image and their calculated theoretical distorted positions. The differences between the corrected positions and the ideal positions are not chosen as the error measure, because the real ideal positions are unavailable. Basically, with the increase of polynomials degrees, the error decreases as a whole except for some small vibrations.

The maximal, minimal, mean and RMS distortion errors for some tests are illustrated in Table 1, in which the polynomial degrees were the degrees for (k_1,k_2,θ,t), respectively, in Eq. (4). Considering the time consumption and acceptable error range, the polynomial degree of (2,2,2,4) was recommended for the distortion correction, in which the RMS error was 0.35 pixels. The results verified the correctness of the proposed distortion correction method.

Accuracy of spatial distance reconstruction

In this experiment, we wanted to test the accuracy of spatial point reconstruction. However, since we did not

Table 1. Results of distortion correction based on the proposed distortion model

Polynomial degree	Distortion correction errors(pixels)			
	Max	Min	Mean	RMS
(2,2,2,2)	1.39	0.04	0.44	0.50
(3,3,2,3)	0.97	0.03	0.35	0.40
(2,2,2,4)	0.93	0.03	0.30	0.35

know the world coordinates of the test points, we reconstructed the Euclidean distance between the spatial points instead. The Euclidean distance is irrelevant to the frame. The small phantom in Figure 6 was used, in which the distance between any two balls could be figured out according to its design. The small phantom was placed on the operation bed. Its images I_0 and I_{30} were captured and corrected based on the C-arm calibration result. The spatial positions were recovered for the balls, which were both visible in I_0 and I_{30}, and the distance between every two balls was calculated.

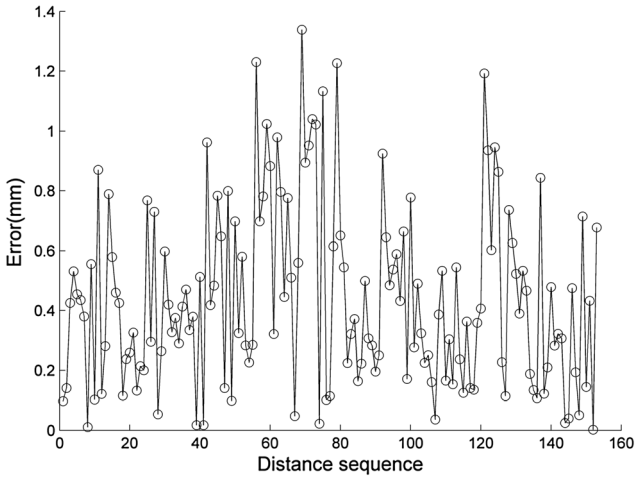

Figure 10. Error curve of distance reconstruction.

Table 2. Spatial distance reconstruction error

Polynomial degree	Reconstruction errors (mm)			
	Max	Min	Mean	RMS
(2,2,2,4)	1.34	0.01	0.44	0.53

The distance reconstruction error was defined as the difference between the reconstructed distance and the corresponding designed distance. As only 18 balls were visible in both images, I_0 and I_{30} in this experiment, there were $C_{18}^2 = 153$ distances reconstructed. The error curve is shown in Figure 10, and the maximal, minimal, mean and RMS error are shown in Table 2. From Table 2, it can be seen that the maximum error was 1.34 mm and RMS was 0.53 mm.

Accuracy of catheter localization

In this experiment, we compared the displacement of the catheter, measured by the encoders in the catheter operator and by IGS. In the catheter operator, encoders were mounted on the driving motors. Supposing that there was no slippage between the catheter and the driving wheels and that the catheter did not deform in the blood vessel, the displacement of the catheter tip could be measured by the encoders.

A glass vascular model filled with distilled water was utilized in this experiment, as in Figure 11. At first, the surgeon teleoperated the robot to push the catheter into the model for a distance, then rotated the catheter without as push movement, then pushed the catheter for another distance. Error in this experiment was defined as the difference between the displacement calculated by the encoders and that calculated by the tip localization by IGS. The errors are shown in Table 3, from which it can be seen that the maximum displacement error of catheter localization was 0.50 mm.

Note that, in a real blood vessel, the resistance of viscous blood and the blood vessel wall may result in slippage and deformation of the catheter, in which case the displacement of the catheter tip in the blood vessel by the encoders may not be accurate; however, this can be avoided by IGS.

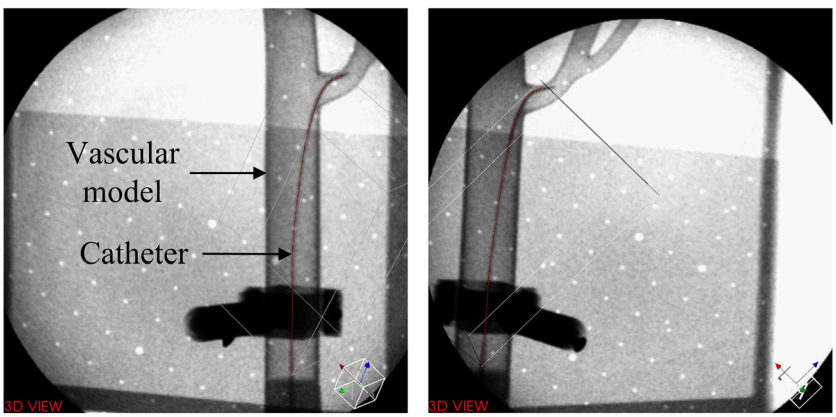

Figure 11. Experiment of catheter localization.

DOI: 10.1002/rcs

Table 3. Error of catheter localization between encoder and IGS

Catheter motion	Δencoder(mm)	Δ_{IGS}(mm)	δ(mm)
Axial insertion	40.63	40.13	0.50
Rotation	0.00	−0.30	0.30
Axial insertion	43.62	43.53	0.09

Clinical simulation and animal experiments

To verify the RVIR's feasibility, it has been tested in an *in vitro* preliminary experiment with a glass vascular model (as shown in Figure 12), and later with animals after the surgeon preliminarily mastered the basic function and operation of the RVIR (as shown in Figure 13). These experiments were presented in detail in (23). The animal trial was carried out under ethical supervision of minimal animal suffering. This trial was approved by, and performed in accordance with, the guidelines of a Beijing hospital.

The vascular model experiment showed that the reconstructed 3D vasculature model was consistent with the form of the practical model. Thus, the IGS can meet interventional requirements and accurately establish 3D model, while providing real-time monitoring of the position and movement of a catheter.

Figure 12. Glass vascular model experiment.

Figure 13. Animal experiment.

In the animal experiments, 10 dogs in total were tested and all returned to normal after palinaesthesia without complications. The animal experiments showed that the surgeon was possible to teleoperate the catheter to carry out invention therapy without radioactive exposure via the RVIR.

Discussion

In the experiments we have tested and determined the image distortion correction error, distance reconstruction error and catheter tip localization error. The accuracy was acceptable by the interventional surgeon at the Navy General Hospital. Several clinical animal tests have been conducted by the surgeon to verify its feasibility. The IGS can not only provide the 3D vasculature model reconstruction and catheter position information, but also overlap the 3D model on the real-time monitoring image to enhance the view. Although the experiments have shown that the RVIR is feasible in VIS, there is still space for improvement:

1. The current RVIR is based on conventional single C-arm DSA machine. Therefore, during the interventional surgery, we should rotate the C-arm to at least two predefined view positions. A dual C-arm machine is becoming general. With a dual C-arm DSA machine, the RVIR can be more effective in saving operation time. However, the discussed technology can be extended to a dual C-arm DSA machine system.
2. In the catheter localization, we still use two views to reconstruct its tip position. However, since the catheter lies in the blood vessel and the 3D vasculature model has been reconstructed, we can trace the catheter tip and add blood vessel constraints to it. Thus, the catheter tip can be located with only one view, i.e. the depth of the tip can be replaced by the depth information of the blood vessel in which the catheter lies. However, this may result in the increase of the tip position error.
3. Since two C-arm views are used to reconstruct the 3D vascular model in IGS, the vascular shape is supposed to be round. To get more accurate vascular shape, more position views should be used. Furthermore, the field of vision of the C-arm is small compared with the whole of the patient's body. To view more of the patient's body, we should move the operation table and repeat the steps. How to merge the 3D models of different body parts is a challenging problem.
4. At present, the force feedback of the RVIR is only fed back to the surgeon by the haptic device. In future work we plan to integrate the touch force information into IGS by visually showing the force direction and magnitude. The feedback force could also be fed back to the robot controller to operate the catheter semi-automatically.
5. The extraction of the blood vessel from the DSA images is conducted manually. This procedure is time-consuming when the structure of a blood vessel is complicated. If the process can be conducted

automatically, it will be more efficient. Furthermore, the IGS cannot yet provide the rotation information of the catheter tip, which needs further work.

Conclusion

We have introduced the system structure of the developed RVIR and its IGS in this paper, mainly about the key technologies in IGS. With the proposed system and method, we managed to perform *in vitro* and *in vivo* VIS tests, using a glass vascular model and animals, respectively.

C-arm calibration and image distortion correction are the basis of IGS. We proposed an automatic method to match the marker on the designed phantom and the image. Then the calibration was done with a non-linear optimization method, based on the revised distortion model, and the image distortion was corrected based on the calibration result. After C-arm calibration and image distortion correction, the 3D vasculature model and 3D position of catheter tip could be reconstructed from DSA images or C-arm images, like traditional stereovision. For the reconstruction, we designed a small phantom and proposed an automatic marker-matching method to calibrate the fundamental matrix between the two views. Finally, the 3D vasculature model could be overlapped on the 2D view image to enhance comparison of 'virtual model' and 'real image'.

The experiments show that the RMS error of distortion correction is 0.35 pixels. For the location error test, we used distance reconstruction error instead to verify the accuracy. The distance measurement with the small phantom showed that the maximum and RMS errors of reconstruction were 1.34 and 0.53 mm, respectively. In the catheter localization test, the catheter displacements by the IGS and by the catheter operator encoder were nearly same, which again verified the accuracy of IGS. The *in vitro* glass model test and clinical animal tests indicated that the RVIR is feasible and valid to help the surgeon perform VIS remotely; the function and reconstruction accuracy of IGS can satisfy the surgeon's requirement to guide the RVIR.

Conflict of interest

The authors have stated explicitly that there are no conflicts of interest in connection with this article.

Acknowledgements

This research was supported by the Chinese NSFC (Grant Nos 60905021 and 61171005), a Chinese High Technology project (Grant No. 2009AA045301-4) and Doctoral Funds of the Chinese Education Ministry (Grant No. 20091102120028).

References

1. Abreu AR, Campos MA, Krieger BP. Pulmonary artery rupture induced by a pulmonary artery catheter: a case report and review of the literature. *J Intensive Care Med* 2004; **5**(19): 291–6.
2. Butner SE, Ghodoussi M. Transforming a surgical robot for human telesurgery. *IEEE Trans. Rob. Autom.* 2003; **19**(5): 818–24.
3. Cleary K, Melzer A, Watson V, Kronreif G, Stoianovici D. Interventional robotic systems: applications and technology state-of-the-art. *Minim Invasive Ther Allied Technol* 2006; **15**(2): 101–13.
4. Guo S, Kondo H, Wang J, Guo J, Tamiya T. A New Catheter Operating System for Medical Applications. Complex Medical Engineering, 2007. CME 2007. IEEE/ICME International Conference on. 2007; 82–6.
5. Hanly EJ, Talamini MA. Robotic abdominal surgery. *Am J Surg* 2004; **188**: 19–26.
6. Munoz V, Vara-Thorbeck C, DeGabriel J, Lozano J, Sanchez-Badajoz E, Garcia-Cerezo A, Toscano R, Jimenez-Garrido A. A medical robotic assistant for minimally invasive surgery. Robotics and Automation, 2000. Proceedings. ICRA'00. IEEE International Conference on. 2000; 2901–6.
7. Liu D, Zhang D, Wang T. Overview of the vascular interventional robot. *Int. J. Med. Rob. Comput. Assisted Surg.* 2008; **4**(4): 289–94.
8. Saliba W, Cummings JE, Oh S, Zhang Y, Mazgalev TN, Schweikert RA, Burkhardt JD, Natale A. Novel robotic catheter remote control system: feasibility and safety of transseptal puncture and endocardial catheter navigation. *J Cardiovasc Electrophysiol* 2006; **10**(17): 1102–5.
9. Jayender J, Azizian M, Patel RV. Autonomous image-guided robot-assisted active catheter insertion. *IEEE Trans. Rob.* 2008; **4** (24): 858–71.
10. Tercero C, Ikeda S, Uchiyama T, Fukuda T, Arai F, Okada Y, Ono Y, Hattori R, Yamamoto T, Negoro M, Takahashi I. Autonomous catheter insertion system using magnetic motion capture sensor for endovascular surgery. *Int. J. Med. Rob. Comput. Assisted Surg.* 2007; **3**(1): 52–8.
11. Tercero C, Ikeda S, Fukuda T, Arai F, Negoro M, Takahashi I. High sensitivity vasculature models and catheter trajectory reconstruction using a bi-planar vision system. Micro-NanoMechatronics and Human Science (MHS), 2011 International Symposium on. 2011; 303–8.
12. Tercero C, Ikeda S, Fukuda T, Arai F, Negoro M, Takahashi I. Numerical comparison of catheter insertion trajectory within blood vessel model using image processing. Micro-NanoMechatronics and Human Science (MHS), 2010 International Symposium on. 2010; 378–83.
13. Tercero C, Ikeda S, Fukuda T, Arai F, Negoro M, Takahashi I. Catheter Insertion Reference Trajectory Construction Method Using Photoelastic Stress Analysis for Quantification of Respect for Tissue During Endovascular Surgery Simulation. *Int. J. Optomechatronics* 2011; **4**(5): 322–39.
14. Liu H, Fu YL, Zhou YY, Li HX, Liang ZG, Wang SG. An in vitro investigation of image-guided steerable catheter navigation. *Proc. Inst. Mech. Eng. Part H J. Eng. Med.* 2010: 945–54.
15. Wang T, Zhang D, Liu D. Remote-controlled vascular interventional surgery robot. *Int. J. Med. Rob. Comput. Assisted Surg.* 2010; **6**(2): 194–201.
16. Mitschke MM, Navab N. Optimal configuration for dynamic calibration of projection geometry of x-ray C-arm systems. Mathematical Methods in Biomedical Image Analysis, 2000. Proceedings. IEEE Workshop on. 2002; 204–9.
17. Yan S, Wang C, Ye M. A method based on moving least squares for XRII image distortion correction. *Med Phys* 2007; **34**: 4194.
18. Cerveri P, Forlani C, Pedotti A, Ferrigno G. Hierarchical radial basis function networks and local polynomial un-warping for X-ray image intensifier distortion correction: A comparison with global techniques. *Med Biol Eng Comput* 2003; **41**(2): 151–63.
19. Gutiérrez LF, Ozturk C, McVeigh ER, Lederman RJ. A practical global distortion correction method for an image intensifier based x-ray fluoroscopy system. *Med Phys* 2008; **35**: 997–1007.
20. Tsai R. A versatile camera calibration technique for high-accuracy 3D machine vision metrology using off-the-shelf TV cameras and lenses. *IEEE J. Rob. Autom.* 1987; **3**(4): 323–44.
21. Hartley R, Zisserman A. Multiple view geometry in computer vision (2nd edn). Cambridge University Press: New York, NY, USA, 2003.
22. Poon K, Hamarneh G, Abugharbieh R. Live-vessel: Extending livewire for simultaneous extraction of optimal medial and boundary paths in vascular images. Medical Image Computing and Computer-Assisted Intervention–MICCAI 2007. 2007; 444–51.
23. Tian Z, Jia B, Lu W, Hui R. Application Study of Vascular Interventional Robotic Mechanism for Remote Steering. *Open Med. Inf. J.* 2011; **5**: 46–9.